Flux-Vector Splitting Calculation of Nonequilibrium Hydrogen-Air Reactions

Seung-Ho Lee*
Eloret Institute, Sunnyvale, California
and
George S. Deiwert†
NASA Ames Research Center, Moffett Field, California

Two methods, fully and loosely coupled, are developed to incorporate nonequilibrium hydrogen-air chemistry into the fluid-dynamic implicit flux-vector splitting code (F3D). The new code (F3D/Chem) is validated against other existing codes for two cases: nozzle expansion and shock-induced combustion around a blunt body. The shock-induced combustion case is compared also with experimental data. The reaction rate constants are varied in an effort to reproduce the experimental data. The fully and loosely coupled methods are found to yield comparable results, but the computation time is shorter using the loosely coupled method. The present method is found to reproduce results obtained using different existing codes. The experimental data were not reproduced with any selected rate coefficients set.

Nomenclature

c_i = mass fraction of species i
c_{p_i} = specific heat of species i
e = total internal energy
h_i = static enthalpy of species i
h_i^0 = heat formation of species i at $T=0$
ns = number of species
k = thermal conductivity
k_r = reaction rate constant
M_∞ = freestream Mach number
R_0 = universal gas constant
T = temperature, K
T_∞ = freestream temperature
u = x-component of velocity
$\tilde{u}_i$ = x-component of diffusion velocity of species i
v = y-component of velocity
$\tilde{v}_i$ = y-component of diffusion velocity of species i
$\bar{W}$ = molecular weight of the mixture
w = z-component of velocity
w_i = molecular weight of species i
$\tilde{w}_i$ = z-component of diffusion velocity of species i
γ = ratio of specific heats
$\bar{\gamma}$ = effective heat ratio of static enthalpy to static internal energy
μ = viscosity
ρ = density
ρ_∞ = freestream density

Introduction

THERE is a resurgence in interest in hypersonic flight. Such interest has led to the re-examination of hypersonic, air-breathing propulsion concepts.[1] Considerable effort is being expended presently to study various aspects of such propulsion concepts. Such studies include numerical simulation of the fluid flows involving fuel/air chemistry in combustion chambers of the supersonic-combustion ram-jet, expanding nozzles, and plumes. To predict the flow properties correctly for such flows, computer codes must accurately capture shock waves and predict the combustion fronts and viscous shear layers in three dimensions.

Most notable among such studies are the works of Drummond,[2] Jachimowski,[3] Oran,[4] Westenberg and Favin,[5] and Shuen and Yoon.[6] The methods of Drummond, Jachimowski, and Oran account for a large number of chemical species and reactions. Their methods are best suited for the subsonic diffusion flames in which a large number of heavy radicals such as HO_2 and H_2O_2 exist. The method of Westenberg and Favin uses a relatively small number of species and reactions and has been applied to the problem of nozzle expansion. Shuen and Yoon used a chemistry model similar to that in the work of Westenberg and Favin.

It is relatively easy to couple the finite-rate chemical processes with the fluid-dynamic algorithm for two-dimensional flows. In two-dimensional implicit methods, there are only two operational factors in the left-hand side of the perfect gas equations. When the chemical reactions are coupled as an additional operational factor, there are three operational factors, which are at least conditionally stable. However, for three-dimensional flows, there could be as many as four operational factors on the left-hand side, for which convergence is doubtful.

There presently exist several known stable techniques for three-dimensional perfect gas flows. One technique is the implicit flux vector splitting method developed by Ying[7] known as F3D. It applies the Steger-Warming flux-vector-splitting technique with upwind differencing in the streamwise direction and central differencing in the crossflow directions, and it accomplishes the three-dimensional spatial integration in a two-factor operation. The method has been verified to be unconditionally stable in three-dimensions. The upwind differencing is numerically dissipative, and the combination of upwind differencing with eigenvalue splitting and transition operators enables capturing of strong embedded shocks. This code has been used successfully to compute the three-dimensional plume flows for a perfect gas.[8]

The first object of this work is to modify the F3D code to incorporate hydrogen-air chemistry. Chemical reactions in the hydrogen-air mixture are important in the study of the combustion chamber, nozzle, and plume flows because hydro-

Presented as Paper 89-1700 at the AIAA 24th Thermophysics Conference, Buffalo, NY, June 12-14, 1989; received July 24, 1989; revision received Nov. 6, 1989.

*Research Scientist. Member AIAA.
†Chief, Aerothermodynamics Branch. Associate Fellow AIAA.

gen is a possible fuel for the supersonic-combustion, ram-jet engines for future hypersonic vehicles such as the National Aero-Space Plane (NASP). The code so developed is named F3D/Chem.

The second object of this work is to determine the validity of the F3D/Chem code. This is accomplished by making code-to-code and code-to-experiment comparisons. The code-to-code comparison is made between the two present methods (fully and loosely coupled) and between the present method and those of others. The code-to-experiment comparison is made for the shock-induced-combustion flow around a blunt body.

Governing Equations

The basic conservation equations for a finite-rate chemically reacting flow are well known. The equations are written in the present work for the generalized orthogonal coordinate system ξ, η, and ζ, where ξ is the streamwise distance, and η and ζ are the two distances normal to the ξ coordinates. The normalized time is expressed by τ. When there is a body, its surface is described by $\zeta=0$. For the viscous region, a thin-layer approximation is used. Thus the governing equations are in the form

$$Q_\tau + E_\xi + F_\eta + G_\zeta = S_\zeta + H$$

where Q is the conservative variable, E, F, and G are the ξ-, η-, and ζ-components of inviscid flux vectors, and S is the viscous flux vector, simplified with the thin-layer approximation. The H variable represents the chemical production rate (source term). The vector Q is chosen in present work to be

$$Q=\frac{1}{J}\begin{pmatrix}\rho\\ \rho u\\ \rho v\\ \rho w\\ e\\ \rho c_i\end{pmatrix}$$

$$i=1,\quad ns-1$$

The quantity ρc_i designates the density of chemical species i, and J is the determinant of the Jacobian matrix for the coordinate transformation from the (x, y, z) to the (ξ, η, ζ) system. The number of chemical species ns is taken to be seven in the present work, as will be explained later.

The inviscid fluxes E, F, and G are

$$E,\ F,\text{ and } G=\frac{1}{J}\begin{pmatrix}\rho\tilde{V}\\ \rho u\tilde{V}+l_x p\\ \rho v\tilde{V}+l_y p\\ \rho w\tilde{V}+l_z p\\ (e+p)\tilde{V}-l_t p\\ \rho c_i\tilde{V}\end{pmatrix}$$

where

$$\tilde{V}=l_t+l_x u+l_y v+l_z w$$

in which l represents the coordinates ξ, η, ζ for E, F, and G, respectively. The chemical production term is given by

$$H=\frac{1}{J}\begin{pmatrix}0\\0\\0\\0\\0\\\dot{w}_i\end{pmatrix}$$

where $\dot{w}_i$ is the source term in the continuity equation of species i. The viscous term is represented by

$$S=\frac{1}{J}\begin{pmatrix}0\\ \mu(\zeta_x^2+\zeta_y^2+\zeta_z^2)u_\zeta+\frac{\mu}{3}(\zeta_x u_\zeta+\zeta_y v_\zeta+\zeta_z w_\zeta)\zeta_x\\ \mu(\zeta_x^2+\zeta_y^2+\zeta_z^2)v_\zeta+\frac{\mu}{3}(\zeta_x u_\zeta+\zeta_y v_\zeta+\zeta_z w_\zeta)\zeta_y\\ \mu(\zeta_x^2+\zeta_y^2+\zeta_z^2)w_\zeta+\frac{\mu}{3}(\zeta_x u_\zeta+\zeta_y v_\zeta+\zeta_z w_\zeta)\zeta_z\\ \left\{\frac{\mu}{2}(\zeta_x^2+\zeta_y^2+\zeta_z^2)(u^2+v^2+w^2)_\zeta\right.\\ +\frac{\mu}{3}(\zeta_x u_\zeta+\zeta_y v_\zeta+\zeta_z w_\zeta)(\zeta_x u_\zeta+\zeta_y v_\zeta+\zeta_z w_\zeta)\\ \left.-(\zeta_x q_x+\zeta_y q_y+\zeta_z q_z)\right\}\\ -(\zeta_x\tilde{u}_i+\zeta_y\tilde{v}_i+\zeta_z\tilde{w}_i)\end{pmatrix}$$

where

$$q_x=-k\frac{\partial T}{\partial x}+\rho\sum_{n=1}^{ns}c_i h_i\tilde{u}_i$$

$$q_y=-k\frac{\partial T}{\partial y}+\rho\sum_{n=1}^{ns}c_i h_i\tilde{v}_i$$

$$q_z=-k\frac{\partial T}{\partial z}+\rho\sum_{n=1}^{ns}c_i h_i\tilde{w}_i$$

The total internal energy is

$$e=\rho\sum_{i=1}^{ns}c_i(h_i+h_i^0)-p+\frac{1}{2}\rho(u^2+v^2+w^2)$$

where the static enthalpy of species i is

$$h_i=\int_{T_0}^{T}c_{p_i}\,dT$$

The pressure is expressed as

$$p=\rho\frac{R_0}{\bar{W}}T$$

where

$$\bar{W}=\left(\sum_{i=1}^{ns}\frac{c_i}{w_i}\right)^{-1}$$

Sample calculations have been made for a viscous flow; however, the calculations presented in this paper were made for the inviscid flow only.

Coupling Methods

The implicit, finite-difference form of the conservation equation is

$$\left[I+\Delta\tau\left(-\frac{\partial H}{\partial Q}+\delta_\xi^b A^+ +\delta_\zeta C-\delta_\zeta M\right)-D_{i\zeta}\right]$$

$$\times[I+\Delta\tau(\delta_\xi^f A^- +\delta_\eta B)-D_{i\eta}]\Delta Q=$$

$$-\Delta\tau[\delta_\xi^b E^+ +\delta_\xi^f E^- +\delta_\eta F+\delta_\zeta G-\delta_\zeta S-H)-D_e Q$$

where δ_η and δ_ζ are the central-differencing operators in the η and ζ directions, and B and C are the inviscid flux Jacobians corresponding to F and G. The symbols δ_ξ^b and δ_ξ^f denote the backward and forward differencing operators in the ξ directions, E^+ and E^- are the components of the inviscid flux vector in the ξ direction corresponding to the positive and the negative eigenvalues, and A^+ and A^- are the corresponding flux Jacobians. $D_{i\zeta}$ and $D_{i\eta}$ are the implicit artificial dissipation operators in the ζ and η directions, and D_eQ is the explicit artificial dissipation term. I is the identity matrix, $\Delta\tau$ is the time step, and $\partial H/\partial Q$ is the source Jacobian.

The split inviscid flux vectors can be expressed as

$$E^{\pm} = (1/J)(E_1\lambda_1^{\pm} + E_4\lambda_4^{\pm} + E_5\lambda_5^{\pm})$$

where

$$E_1 = \frac{\rho(\bar{\gamma}-1)}{\bar{\gamma}} \begin{bmatrix} 1 \\ u \\ v \\ w \\ \dfrac{u^2+v^2+w^2}{2} + \displaystyle\sum_{i=1}^{ns} c_i h_i^0 \\ c_i \end{bmatrix}$$

$$E_4 = \frac{\rho}{2\bar{\gamma}} \begin{bmatrix} 1 \\ u + \dfrac{a\xi_x}{\sqrt{\xi_x^2+\xi_y^2+\xi_z^2}} \\ v + \dfrac{a\xi_y}{\sqrt{\xi_x^2+\xi_y^2+\xi_z^2}} \\ w + \dfrac{a\xi_z}{\sqrt{\xi_x^2+\xi_y^2+\xi_z^2}} \\ \dfrac{u^{+2}+v^{+2}+w^{+2}}{2} + \displaystyle\sum_{i=1}^{ns} c_i h_i^0 + \frac{3-\bar{\gamma}}{2(\bar{\gamma}-1)} a^2 \\ c_i \end{bmatrix}$$

$$E_5 = \frac{\rho}{2\bar{\gamma}} \begin{bmatrix} 1 \\ u - \dfrac{a\xi_x}{\sqrt{\xi_x^2+\xi_y^2+\xi_z^2}} \\ v - \dfrac{a\xi_y}{\sqrt{\xi_x^2+\xi_y^2+\xi_z^2}} \\ w - \dfrac{a\xi_z}{\sqrt{\xi_x^2+\xi_y^2+\xi_z^2}} \\ \dfrac{u^{-2}+v^{-2}+w^{-2}}{2} + \displaystyle\sum_{i=1}^{ns} c_i h_i^0 + \frac{3-\bar{\gamma}}{2(\bar{\gamma}-1)} a^2 \\ c_i \end{bmatrix}$$

$$\lambda_{1,4,5} = U, \quad U + a\sqrt{\xi_x^2+\xi_y^2+\xi_z^2}, \quad U - a\sqrt{\xi_x^2+\xi_y^2+\xi_z^2}$$

$$\lambda_{1,4,5}^{\pm} = \frac{\lambda_{1,4,5} \pm |\lambda_{1,4,5}|}{2}$$

and the speed of sound is defined as

$$a = \sqrt{\bar{\gamma}(p/\rho)}$$

The general flux Jacobians A^+, A^-, B, and C consist of four parts: the part that represents the variations in fluid dynamic fluxes due to the changes in fluid dynamic variables (A_F), the part that represents the variations in fluid dynamic fluxes due to the changes in chemical species (A_{FC}), the part that represents the variations in chemical species fluxes due to the changes in fluid dynamic variables (A_{CF}), and the part that represents the changes in chemical species due to the changes in the chemical species (A_C). The components A_{FC} and A_{CF} represent the coupling between the chemical reactions and the fluid motion. When all these four parts are retained and correctly calculated, the solutions are unquestionably accurate. If the coupling between the fluid motion and chemical reactions is weak, the elements in the flux Jacobian containing the fluid-chemistry coupling (A_{FC}) may be neglected.

In this study two different computing methods are developed to treat the coupling between the chemical reactions and the fluid dynamics, namely, a fully coupled and a loosely coupled method. The fully coupled method accounts fully for all four parts in the flux Jacobians and carries out time integration by inverting the complete block tridiagonal system of the matrices of the order $4+ns$ in three dimensions.

For steady-state calculations, we may use the loosely coupled approach that neglects A_{FC}. Neglecting A_{FC} is equivalent to the assumption that the effective specific heat ratio and pressure are not affected by the changes in species mass fractions. In this scheme, the coupling between fluid dynamics and chemistry appears only in the flux Jacobian elements of the chemical variables, A_{CF}. The A_{CF} component cannot be neglected because density ρ appears in the expression for species variables ρc_i. The fluid dynamic variables can be computed first using the local values of the specific heat ratios, and the chemical variables can be computed next with the coupling terms A_{CF} moved to the right-hand sides of the species conservation equations in integration. Then, the chemistry part of the previous equation with the coupling terms, subscripted with CF, can be rewritten as

$$\left[I + \Delta\tau\left(-\frac{\partial H}{\partial Q} + \delta_\xi^b A^+ + \delta_\zeta C - \delta_\zeta M\right) - D_{i\zeta}\right]_C \times [I + \Delta\tau(\delta_\xi^f A^- + \delta_\eta B) - D_{i\eta}]_C \Delta Q_C =$$

$$-\Delta\tau[\delta_\xi^b E^+ + \delta_\xi^f E^- + \delta_\eta F + \delta_\zeta G - \delta_\zeta S - H]_C - D_e Q_C$$

$$-\Delta\tau[\delta_\xi^b A^+ + \delta_\zeta C + \delta_\xi^f A^- + \delta_\eta B]_{CF} \Delta Q_F$$

where ΔQ_C and ΔQ_F represent the difference of the chemical variables and the fluid dynamic variables between a time step $\Delta\tau$. This method requires the inversion of a block tridiagonal system corresponding to two smaller matrices instead of a single large matrix, one of order of 5 (for three dimensions) and the other of $ns-1$. This reduces the required computation time.

Chemistry Model

A computer code, F3D/Chem, has been written for a generalized chemistry model so that any chemistry model of the hydrogen-air system can be accepted. For the purpose of the present study, a chemistry model involving seven species (H, H_2, H_2O, O, OH, O_2, and N_2) and eight reactions is used. N_2 is treated as an inert gas.

The reactions considered are

$$H + O_2 \rightleftharpoons OH + O \quad (1)$$

$$O + H_2 \rightleftharpoons OH + H \quad (2)$$

$$O + H_2O \rightleftharpoons OH + OH \quad (3)$$

$$H + H_2O \rightleftharpoons OH + H_2 \quad (4)$$

$$H_2 + M \rightleftharpoons H + H + M \quad (5)$$

$$O_2 + M \rightleftharpoons O + O + M \quad (6)$$

$$OH + M \rightleftharpoons O + H + M \quad (7)$$

$$H_2O + M \rightleftharpoons OH + H + M \quad (8)$$

The rate coefficients for these reactions are expressed in the endothermic form in the present work. Several different sets of rate coefficients are used. Most calculations are made using one of the three reaction rate sets given in Table 1, models 1, 2, and 3. Model 1 is based on the work of Dash and Pergament[9] and is believed to best describe the expanding flows in nozzles and plumes. In this model, the original rate coefficient values are given in the exothermic form. The endothermic rate coefficients are deduced from the equilibrium relationship in the present work. Model 2 is taken from the work of Evans and Schexnayder[10] and is believed to be appropriate for diffusion flames. Model 3 is taken from the review by Cohen and Westberg[11] and is the most up to date. As will be elaborated later (code-to-experiment comparison), model 3 is considered to be the standard.

As mentioned earlier, Drummond, Jachimowski, and Oran used more complicated reaction models than the present model because HO_2 and H_2O_2 were included. However, in the temperature range of interest in the present work, such species are unimportant. When HO_2 and H_2O_2 are excluded from the consideration, the chemistry model of Drummond and Oran are similar to the present model. The chemistry model used in the work of Westenberg and Favin and by Shuen and Yoon are very similar to the present model.

The chemistry models used in the present work and by others are subject to considerable uncertainty. In all models, the expressions for the reaction-rate coefficients have been obtained by fairing a smooth curve through two totally different groups of experimental data, namely, those from shock tube and from the microwave experiments. Shock-tube data are for temperatures above 2000 K and are obtained in an environment in which the internal degrees of freedom are excited to less than the equilibrium values. Microwave data have been obtained for temperatures below 500 K and are obtained in an environment in which the internal degrees of freedom are excited to more than the equilibrium values. Shock tube data tend to underestimate the rate coefficients; whereas microwave data tend to overestimate the rate coefficients. In a shock-tube experiment, a chemical reaction is usually preceded by an induction period during which the internal degrees of freedom are being excited. However such an induction phenomenon is ignored in the description of the rate processes.

For the calculation of species-specific heat, the thermodynamic data and their curve fit coefficients developed at the NASA Lewis Research Center[14,15] are used.

No effort was made to vectorize any part of the code.

Table 1 Reaction rate coefficients for models 1, 2, and 3[a]

	Model 1: $k_r = AT^{-n}\exp(E/RT)$		
	A	n	E
Reaction 1b[b]	3.00×10^{-11}	0.0	−960.0
Reaction 2b	1.40×10^{-14}	−1.0	−7000.0
Reaction 3b	1.00×10^{-11}	0.0	−1100.0
Reaction 4b	3.50×10^{-11}	0.0	−7000.0
Reaction 5b	3.00×10^{-30}	1.0	0.0
Reaction 6b	3.00×10^{-34}	0.0	1800.0
Reaction 7b	1.00×10^{-29}	1.0	0.0
Reaction 8b	1.00×10^{-25}	2.0	0.0
	Model 2: $k_r = AT^{-n}\exp(C/T)$		
	A	n	C
Reaction 1f[c]	2.20×10^{14}	0.0	−8455.0
Reaction 2f	7.50×10^{13}	0.0	−5586.0
Reaction 3f	5.30×10^{12}	0.0	−503.0
Reaction 4f	2.00×10^{13}	0.0	−2600.0
Reaction 5f	5.50×10^{18}	1.0	−51987.0
Reaction 6f	7.20×10^{18}	1.0	−59340.0
Reaction 7b	7.10×10^{18}	1.0	0.0
Reaction 8b	4.40×10^{20}	1.5	0.0
	Model 3: $k_r = AT^{-n}\exp(C/T)$		
	A	n	C
Reaction 1f	1.67×10^{17}	0.9	−8750.0 (Ref. 11)
Reaction 2f	1.10×10^{4}	−2.8	−2980.0 (Ref. 11)
Reaction 3f	4.60×10^{9}	−1.3	−8605.0 (Ref. 11)
Reaction 4f	6.20×10^{7}	−1.9	−9265.0 (Ref. 11)
Reaction 5f	4.58×10^{19}	1.4	−52530.0 (Ref. 11)
Reaction 6f	3.60×10^{18}	1.0	−59380.0 (Ref. 13)
Reaction 7b	4.72×10^{18}	1.0	0.0 (Ref. 12)
Reaction 8b	2.21×10^{22}	2.0	0.0 (Refs. 11,13)

[a] k_r = cm³/molecule-s or cm⁶/molecule²-s in model, and cm³/mol-s or cm⁶/mol²-s in models 2 and 3. [b] b = backward reaction. [c] f = forward reaction.

Code-to-Code Validation

Fully Coupled vs Loosely Coupled for a 31-Deg Ramp

The F3D/Chem code was run first for the flow over a 31-deg ramp for the purpose of comparing the loosely coupled method with the fully coupled method. The freestream conditions were as follows: pressure = 0.06 atm, temperature = 840 K, Mach number = 3.8, and equivalence fuel ratio = 0.6. The computing domain consists of a rectangle 30 × 20 cm in size. A 57 × 41-mesh grid was used. The rate coefficients of model 1 in Table 1 were used for this case. The inviscid boundary condition was implemented by specifying zero gradient in density, pressure, and species density and velocity slip at the wall.

The computation times required are found to be approximately 3.2 and 1.9 ms per node point per time step for the fully and the loosely coupled methods, respectively, on the CRAY-2 computer.

The density contours obtained from the solution are shown in Fig. 1. The two methods, fully and loosely coupled, yielded almost (to four significant figures) identical values in all flow properties.

The convergence history is shown in Fig. 2. The figure shows the changes in $L2$ norm, which is the root-mean square of the magnitudes of the residuals in the right side of the difference equation. As the figure shows, both methods converge almost monotonically each to a very small value. The fully coupled method converges at a faster rate than the loosely coupled method. However, since the loosely coupled method requires only about 70% as much time as the fully coupled method per time step, the total computing time required is less for the loosely coupled method. Typically the loosely coupled method requires about two-thirds of the computing time for the fully coupled method.

Loosely Coupled vs APL Gennoz and SPARK Codes for a Nozzle Flow

Next, the loosely coupled method was applied for the flow through a nozzle for the purpose of comparing with other existing codes. The geometry of the tested nozzle is shown in Fig. 3a. The grid contains 41 meshes along the nozzle axis and 16 meshes in the transverse direction. The inflow conditions at the throat of the nozzle ($x = 7.08$ cm) are as follows: pressure = 56.4 atm, temperature = 3013.0 K, velocity = 1196.0 m/s, density = 55.507 kg/m³, and throat radius = 1.5244 cm. Species mass fractions are $H = 4.3200\times10^{-4}$, $H_2 = 1.0220\times$

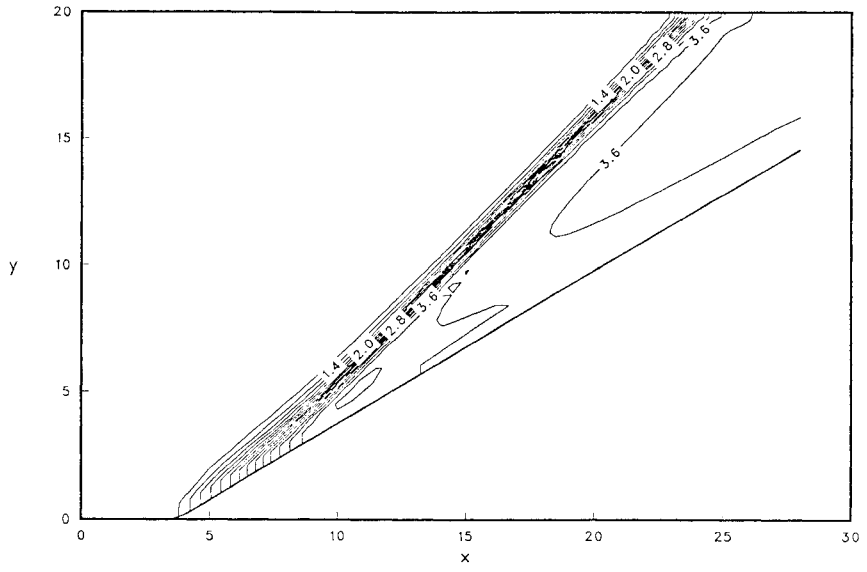

Fig. 1 The density contours for a 31-deg ramp using the fully and loosely coupled methods.

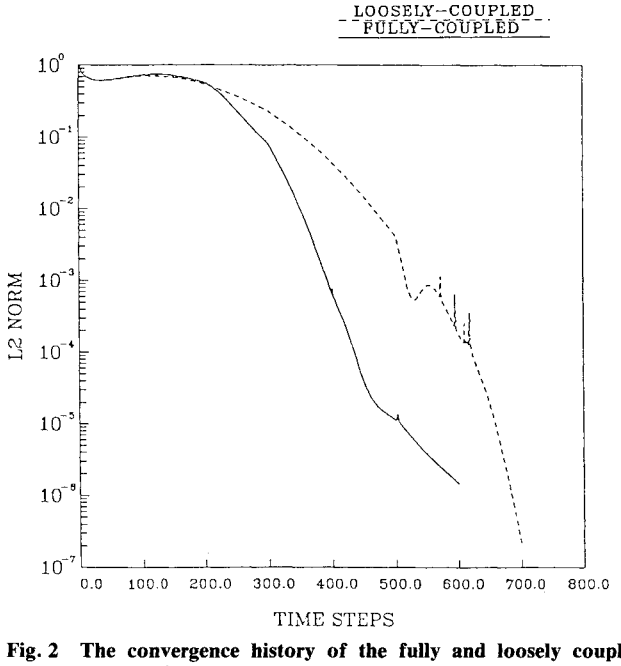

Fig. 2 The convergence history of the fully and loosely coupled methods for the 31-deg ramp case.

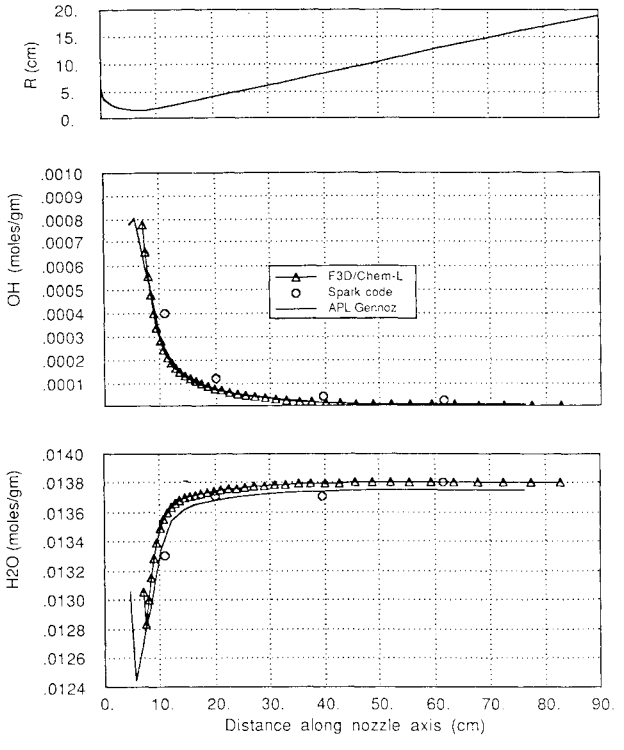

Fig. 3 Nozzle wall geometry and the OH and H_2O concentrations along the nozzle axis.

10^{-3}, $H_2O = 2.3512 \times 10^{-1}$, $O = 1.7240 \times 10^{-3}$, $OH = 1.3198 \times 10^{-2}$, $O_2 = 3.8700 \times 10^{-3}$, and $N_2 = 7.4463 \times 10^{-1}$.

The same case had been computed previously at the NASA Ames Research Center using other existing codes.[5,16] These results are compared with the present results in Figs. 3b and 3c. The present results are in close agreement with the results of the APL Gennoz code,[5] which uses a similar chemistry model. The present results are in fair agreement with the results of the SPARK[16] code, which uses a chemistry model substantially different from the present model.

Loosely Coupled vs Yungster's Solution for a Shock-Induced Combustion Problem

Next, the calculation was repeated for the shock-induced-combustion flow over a blunt body. The blunt body is a sphere cylinder with a nose radius of 7.5 mm. It flies through a stoichiometric hydrogen-air mixture at a pressure of 0.421 atm with a speed of 2605 m/s (Mach number 6.46). Its speed is much greater than the detonation speed of the gas mixture (2055 m/s at this condition). The reaction rate coefficients were taken from Evans and Schexnayder.[10] The flowfield of the sphere cylinder was computed with a grid with 57×41 meshes (41 in the radial direction). The length of the cylindrical section is assumed to be 0.42 times the radius of the sphere.

Yungster et al.[17] calculated the same flowfield using the total variation diminishing (TVD) algorithm of Yee and Shinn.[18] The chemistry model and the rate coefficients used by Yungster et al. are the same as in the present code.

Figures 4a and 4b compare the temperature distribution obtained by the present computation with that by Yungster et al. The two results are in good agreement.

Code-to-Experiment Comparison

Next, the present code is compared with an experimental result. An experiment was performed previously by Lehr for

shock-induced combustion.[19] In this experiment, a sphere-cylinder model was flown into an ambient atmosphere consisting of stoichiometric hydrogen-air mixture in a ballistic range. The dimensions of the model and the flight conditions were those given earlier (loosely coupled vs Yungster's solution for a shock-induced combustion problem). The schlieren photograph of the flowfield obtained is reproduced in Fig. 5. The photograph shows two distinct density demarcations. The outer demarcation is the familiar bow shock wave. The inner demarcation is interpreted by Lehr to be due to the combustion or flame front. The combustion front is visible in the schlieren photograph because of the sudden change in temperature and density accompanying oxidation of hydrogen. In the stagnation region, the combustion front and the shock wave converge. In this region, the normal component of the velocity for the combustion front is greater than the Chapman-Jouguet detonation velocity, and therefore the combustion front is interpreted to be a deflagration wave.[19] The two waves separate from each other at the point where the normal component of the velocity is equal to the detonation velocity.

The kinetics of the shock-induced combustion is initiated by the dissociation of H_2 by the shock wave, reaction 5 in the list of reactions given earlier. The atomic H so produced reacts with O_2 to yield OH and the atomic O through reaction 1. The bimolecular reaction (reaction 2) follows to produce more radical species H at OH. H_2O is formed through the bimolecular reactions 3 and 4, and the recombination process 8. Therefore the most important reactions are the dissociation of H_2, reaction 5, and the bimolecular reaction, reaction 1.

To calculate this shock-induced combustion problem, the reaction rate coefficients selected first from the shock tube experiments were adopted. For the rate coefficients of the dissociation of H_2 and O_2, the lowest values were picked from the available data.[13] Also the lowest value of the bimolecular reaction of the atomic H and the O_2 (reaction 1) was picked. The values recommended by Cohen and Westberg[11] were used for the rest of the reaction rate coefficients. This set of reaction rate coefficients will be referred to as the standard set and is identified as model 3 in Table 1.

Four different cases were calculated by varying the rate coefficients: the case in which the standard set of reaction rate coefficients is used (standard case), the frozen flow, and two cases where slower reaction rates are used (*cs*1 and *cs*2). The rate coefficients for the frozen flow and the *cs*1 cases are obtained by multiplying the standard set values by 0.01 and 0.1, respectively. For the *cs*2 case, only the rate coefficient for reaction 1 is multiplied by 0.1.

The computed flow density ratios are shown for the standard case in Fig. 6a. The density ratio varies from the freestream value of unity to 5.6 immediately behind the normal shock. The ratio decreases toward the stagnation point due to combustion. In the oblique region of the bow shock wave, the density ratio jumps to a high value, such as 4, immediately behind the shock wave. It also decreases monotonically toward the wall as combustion proceeds. However, there is no sudden change in density (combustion front) implied in the schlieren photograph of Fig. 5.

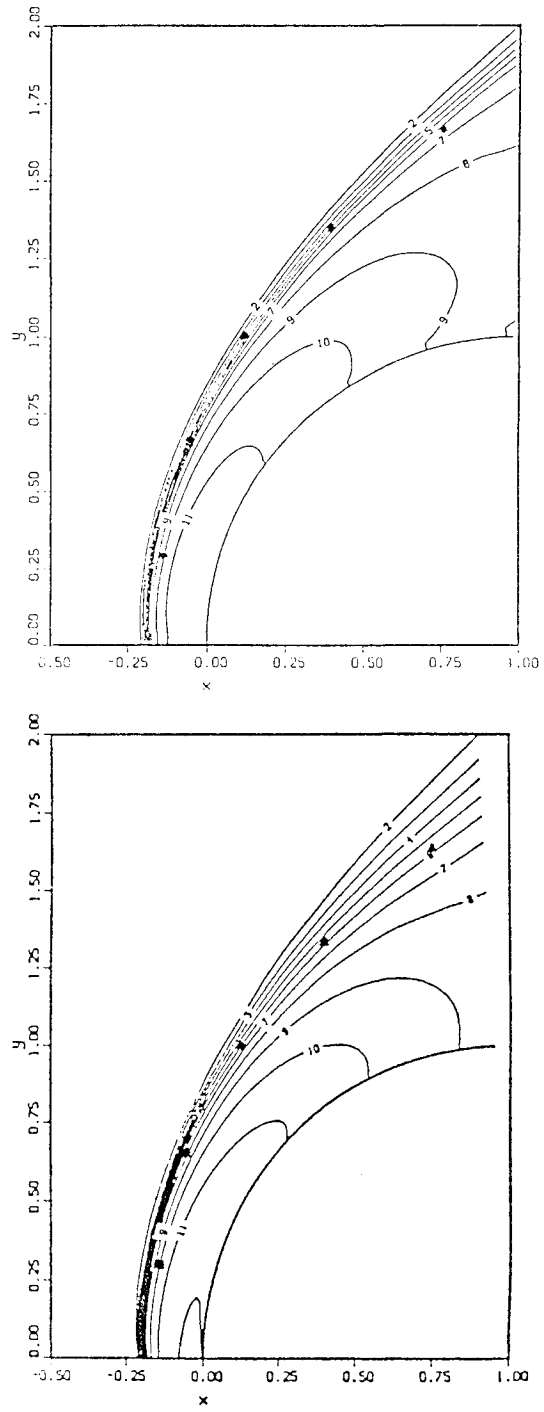

Fig. 4 Temperature contours (T/T_∞) for stoichiometric H_2/air at $M_\infty = 6.46$ of a) present solution and b) Yungster's solution.

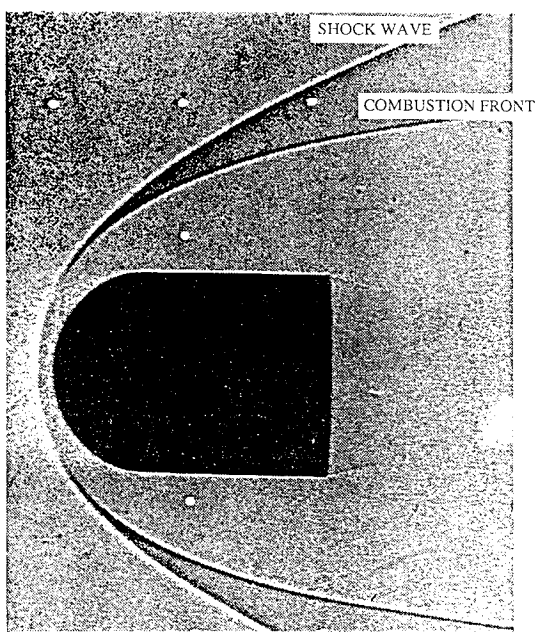

Fig. 5 The schlieren photograph of shock deflagration around a blunt body with a superdetonative speed in a stoichiometric H_2/air mixture.

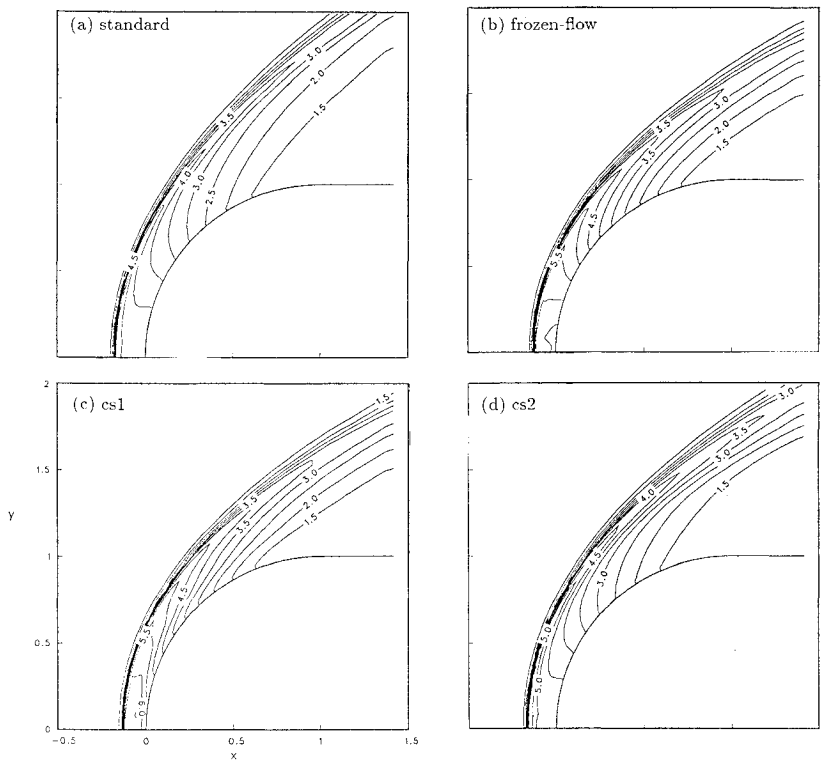

Fig. 6 The density (ρ/ρ_∞) contours for the four cases of stoichiometric H_2/air at $M_\infty = 6.46$.

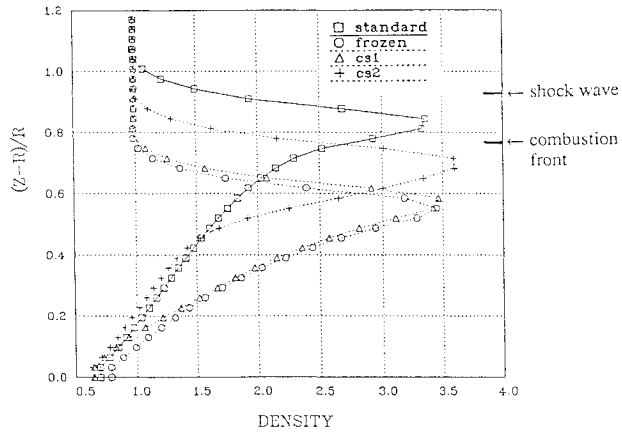

Fig. 7 The density (ρ/ρ_∞) distributions along the radial distance at the shoulder of a sphere-cylindrical body for stoichiometric H_2/air at $M_\infty = 6.46$.

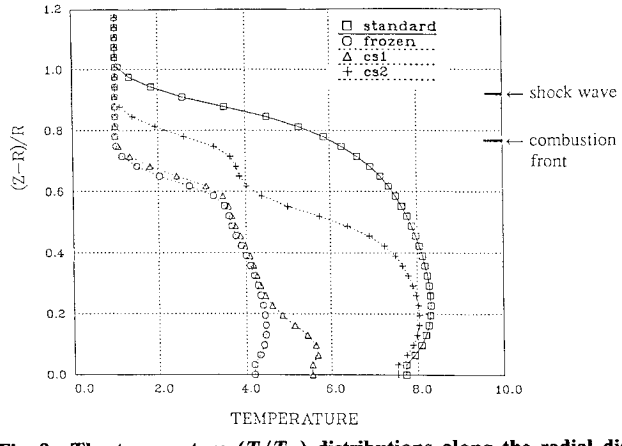

Fig. 8 The temperature (T/T_∞) distributions along the radial distance at the shoulder of a sphere-cylindrical body for stoichiometric H_2/air at $M_\infty = 6.46$.

The density contours for the frozen flow, *cs*1, and *cs*2 cases are shown in Figs. 6. For the frozen-flow case, the shock standoff distance is generally smaller than for the standard case not only in the normal shock region but also on the oblique shock region. In the normal shock region, the shock standoff distance is approximately 14% of the body radius. This agrees closely with the value for the perfect gas of $\gamma = 1.4$ for this Mach number. For the *cs*1 case, the general tendency is the same as for the standard case. The shock standoff distance is between the standard case and the frozen-flow case as expected. For the *cs*2 case, a small region of density plateau is seen between the shock wave and the body. Density decrease occurs behind the plateau with a modest gradient. This density change can be interpreted to be the combustion front. However, the combustion front is not as sharp as in the experimental data. Moreover, the location of the combustion front does not agree with the experimental data: the combustion front is almost parallel to the shock wave instead of being divergent as seen in the experimental data. The location of the shock wave is closer to the body than in the experimental data.

Figure 7 shows the density ratio for the four cases along a radial distance. In the figure, the abscissa are the density ratio, and the ordinates are the radial distances from the sphere-cylinder juncture point, normalized by the body radius. The figure shows that the peak values of the density ratio are about 3.5 for all cases, but their locations are significantly different. This indicates that the flowfield is sensitive to the choice of reaction rate coefficients. The peak point is the closest to the body for the frozen flow and the farthest for the standard case. This is understandable: chemical reactions cause the density within the shock layer to decrease and thereby cause the shock envelope to enlarge. For each curve, the region of fastest increase in density can be interpreted to be the combustion front, and the region of fastest decrease can be interpreted to be the shock wave. The locations of the shock wave and the combustion front agree approximately with the experimental data for the standard case. For the standard, frozen-flow, and the *cs*1 cases, there are virtually no plateaus in density between the shock wave and the combustion front—meaning that the combustion front immediately fol-

lows the shock wave. This point disagrees with the experimental data: in the experiment, there seems to be a fairly broad region of constant property between the shock wave and the combustion front. This discrepancy between theory and experiment can be interpreted to mean that the calculated chemical reactions occur faster than those observed experimentally. Only for the *cs*2 case, there is a small region of density plateau, in qualitative agreement with the experimental data. However, the locations of the shock wave and the combustion front do not agree with the experimental data.

Figure 8 shows the temperature distribution in the same format. The figure shows lower temperature for smaller reaction rate coefficients, as expected. In this plot, both shock wave and combustion front increase temperature. For the standard case, the temperature rise is monotonic, and, therefore, one cannot distinguish where the shock wave ends and the combustion front starts. Thus this figure corroborates Fig. 7 to show that, for the standard case, the combustion front starts immediately behind the shock wave. Only for the *cs*2 case, there is a small region of temperature plateau that separates the combustion front from the shock wave. This again corroborates Fig. 7. As in Fig. 7, the locations of the shock wave and the combustion front disagree with the experimental data.

Although not shown in this paper, calculations were also made with several other sets of reaction rate coefficient values in an effort to reproduce the experimental data numerically. It was found that the experimental data could not be reproduced numerically using any of the reaction rate coefficient sets tried in this effort.

Discussion

The preceding code-to-code comparison indicates that the F3D/Chem code is at least equivalent to other existing reacting-flow codes. The frozen-flow solution for the sphere cylinder correctly reproduced the perfect-gas shock standoff distance indicating the accuracy of the computational fluid dynamics algorithm. The code-to-experiment comparison indicates that the chemical reactions occur generally slower than calculated, even when the calculation is made using the smallest plausible rate coefficient values. Therefore, the failure to reproduce the experimental data cannot be attributed to the computational inaccuracy. As seen in Figs. 7 and 8, the flowfield is affected substantially by the chemical reactions. Therefore, the failure to reproduce the experimental data is believed to be due to the failure to correctly reproduce the chemical reactions.

There are two possible causes for the failure of the chemical reaction model. First, the seven-species model used in the present work may be inadequate: the neglected species such as HO_2 and H_2O_2 may affect the reactions even though their concentrations may be very small at the high temperatures considered in the present work. Second, nonequilibrium of the internal degrees of freedom for the species may affect the reaction rates. For instance, according to Myerson and Watt,[20] there is an induction time of as long as 70 μs preceding the dissociation of H_2 at an ambient pressure of 13 Torr and postshock temperature of 2000 K. Such a long induction time could explain the observed delay of the combustion front. The induction process may be associated with the nonequilibrium rotation, vibration, and electronic excitation processes.

Conclusions

A computer code (F3D/Chem) has been developed, which calculates nonequilibrium chemical reactions in three dimensions employing an implicit two-factored flux-vector-splitting scheme for the calculation of the flow of hydrogen-air mixture. Chemistry is coupled with the fluid motion by either a fully or a loosely coupled method. The two methods yield the same results, but the loosely coupled method is faster. The developed code is numerically at least as accurate as other existing codes. However, the existing shock-induced combustion experimental data cannot be reproduced using the present model, even when the reaction rate coefficients are changed.

Acknowledgments

The authors express their thanks to Mr. G. Palmer of the NASA Ames Research Center and Dr. D. W. Bogdanoff of the Eloret Institute for providing the nozzle flow solution using SPARK and APL Gennoz codes, shown in Figs. 3b and 3c. The first author was supported by NASA Grant NCC2-420, through the Eloret Institute.

References

[1]Anderson, J. D., "A Survey of Modern Research in Hypersonic Aerodynamics," AIAA Paper 84-1578, June 1984.

[2]Drummond, J. P., Rogers, R. C., and Hussaini, M. Y., "A Detailed Numerical Model of a Supersonic Reacting Mixing Layer," AIAA Paper 86-1427, June 1986.

[3]Jachimowski, C. J., "An Analytical Study of the Hydrogen-Air Reaction Mechanism With Application to Scramjet Combustion," NASA TP-2791, Feb. 1988.

[4]Oran, E., Young, T., and Boris, J., "Application of Time-Dependent Numerical Methods to the Description of Reactive Shocks," *Proceedings of the 17th International Symposium of Combustion,* The Combustion Inst., Pittsburgh, PA, 1978, pp. 43–54.

[5]Westenberg, A. A., and Favin S., "Complex Chemical Kinetics in Supersonic Nozzle Flow," *Proceedings of the 9th International Symposium on Combustion,* The Combustion Inst., Pittsburgh, PA, 1963, pp. 785–798.

[6]Shuen, J. S., and Yoon, S., "Numerical Study of Chemically Reacting Flows Using an LU Scheme," AIAA Paper 88-0436, Jan. 1988.

[7]Ying, S. X., "Three-Dimensional Implicit Approximately Factored Schemes for the Equations of Gasdynamics," Ph.D. Thesis, Stanford Univ., Stanford, CA, June 1986.

[8]Venkatapathy, E., and Feiereisen, W. J., "3-D Plume Flow Computations with an Upwind Solver," AIAA Paper 88-3158, July 1988.

[9]Dash, S. M., and Pergament, H. S., "The JANNAF Standard Plume Flowfield Model: Operational Features and Preliminary Assessment," *JANNAF 12th Plume Technology Meeting,* Vol. 2, Colorado Springs, CO, Nov. 1980, pp. 225–288.

[10]Evans, J. S., and Schexnayder, C. J., "Influence of Chemical Kinetics and Unmixedness on Burning in Supersonic Hydrogen Flames," *AIAA Journal,* Vol. 18, No. 2, 1980, pp. 188–193.

[11]Cohen, N., and Westberg, K., "Chemical Kinetic Data Sheets for High-Temperature Chemical Reactions," *Journal of Physical and Chemical Reference Data,* Vol. 12, No. 3, 1983, pp. 531–590.

[12]Tsang, W., and Hampson, R. F., "Chemical Kinetic Data Base for Combustion Chemistry. Part I. Methane and Related Compounds," *Journal of Physical and Chemical Reference Data,* Vol. 15, No. 3, 1986, pp. 1087–1279.

[13]Baulch, D. L., Drysdale, D. D., Horne, D. G., and Lloyd, A. C., *Evaluated Kinetic Data for High Temperature Reactions, Vol 1: Homogeneous Gas Phase Reactions of the H_2-O_2 System,* Butterworths, London, 1972.

[14]Gordon, S., and McBride, B. J., "Computer Program for Calculation of Complex Chemical Equilibrium Compositions, Rocket Performance, Incident and Reflected Shocks, and Chapman-Jouguet Detonations," NASA SP-273, 1976.

[15]Gordon, S., McBride, B. J., and Zeleznik, F. J., "Computer Program for Calculation of Complex Chemical Equilibrium Compositions and Applications Supplement I—Transport Properties," NASA TM-86885, 1984.

[16]Drummond, J. P., and Weidner, E. H., "Numerical Study of Staged Fuel Injection for Supersonic Combustion," *AIAA Journal,* Vol. 20, No. 9, 1982, pp. 1182–1187.

[17]Yungster, S., Eberhardt, S., and Bruckner, A. P., "Numerical Simulation of Shock-Induced Combustion Generated by High-Speed Projectiles in Detonable Gas Mixtures," AIAA Paper 89-0673, Jan. 1989.

[18]Yee, H. C., and Shinn, J. L., "Semi Implicit and Fully Implicit Shock-Capturing Methods for Hypersonic Conservation Laws with Stiff Source Terms," NASA TM-89415, Dec. 1986.

[19]Lehr, H. F., "Experiments on Shock-Induced Combustion," *Astronautica Acta,* Vol. 17, 1972, pp. 589–597.

[20]Myerson, A. L., and Watt, W. S., "Atom-Formation Rates behind Shock Waves in Hydrogen and the Effect of Added Oxygen," *Journal of Chemical Physics,* Vol. 49, July 1968, pp. 425–433.

Clark H. Lewis
Associate Editor